Retrieval of Composite Model Parameters for 3-D Microwave Imaging of Biaxial Objects by BCGS-FFT and PSO

Jiawen Li, Jianliang Zhuo, Yanjin Chen, Feng Han, *Member, IEEE*, and Qing Huo Liu, *Fellow, IEEE*

***Abstract*— This article presents the 3-D quantitative microwave imaging of homogeneous biaxial anisotropic objects with their optical axes being in arbitrary directions. Two sets of model parameters, the anisotropic dielectric parameters and the angles of optical axes with respect to the user-defined coordinate system, are retrieved iteratively. In the forward model, the total fields are solved from the discretized combined field volume integral equations (CFVIEs) by the stabilized biconjugate gradient fast Fourier transform (BCGS-FFT) method. In the inversion model, the optimized solutions for two sets of model parameters are obtained by the particle swarm optimization (PSO) method. If the geometric models of the homogeneous anisotropic objects are unknown, a full-wave inversion method, the variational Born iterative method (VBIM), is combined with the multiparametric structural consistency constraint (SCC) to find the spatial boundaries of the homogeneous objects in advance. Two numerical examples are used to test the proposed method, and the results show that BCGS-FFT-PSO not only has strong adaptability for optical axes angles varying in wide ranges but also can retrieve composite model parameters of multiple homogeneous biaxial objects simultaneously even when the measured data are contaminated by noise.**

***Index Terms*— Biaxial anisotropy, microwave imaging (MWI), particle swarm optimization (PSO), stabilized biconjugate-gradient fast Fourier transform (BCGS-FFT).**

I. Introduction

MICROWAVE imaging (MWI) techniques have been developed significantly over the past decades. According to the application requirements, MWI can be categorized into two types, the qualitative imaging and the quantitative imaging. Qualitative MWI only gives the approximate shapes and locations of the unknown targets and has the obvious advantage of low computational cost. One of its popular applications is the high-frequency tomography. For example, in [1], a clinical prototype of the medical MWI system was developed to diagnose the breast cancer. Afsari *et al.* [2] proposed a fast medical microwave tomography algorithm which could be potentially used during medical emergency such as professional sports or road accidents. The back-projection (BP) tomography [3] and diffraction tomography [4] were adopted in the real-time through-the-wall imaging. Another application is the synthetic aperture radar (SAR). It has been used to image the earth surface [5], [6] or detect the moving target [7]. In addition, the qualitative MWI was also utilized in migration for geophysical prospecting [8]–[10]. However, qualitative MWI shows only images of the targets, and cannot be used to retrieve their dielectric properties.

On the other hand, we can obtain more model parameters of the unknown targets including shapes, positions, dielectric parameters, etc., by using quantitative MWI techniques. Usually, full-wave inversion (FWI) methods must be adopted in order to reconstruct the permittivity, permeability as well as conductivity of the target. Most commonly used FWI methods include Born iterative method (BIM) and its variants, contrast source inversion (CSI), subspace optimization method (SOM), etc. Previously, several related studies have been done not only to check their feasibility in numerical examples but also, to verify them in laboratory experiments. In [11], the preconditioned CSI was used to reconstruct the 2-D profiles for the breast tumor detection. Later, 3-D images of dielectric balls were reconstructed from experimental data using BIM [12]. Similar quantitative MWI laboratory experiments were performed in [13] and [14] but the CSI was used. In [15], distorted BIM (DBIM) and SOM were, respectively, used to obtain the homogeneous and inhomogeneous dielectric parameter distributions in a certain region. These iterative inversion methods are called deterministic methods since the solvers try to find the most optimized solutions by following a fixed iterative way. There is another type of electromagnetic inversion, the stochastic method, which has also been applied to MWI. For example, the genetic algorithm (GA) has been used to reconstruct a pixel-based 2-D image of a cylinder [16] and retrieve the multiple parameters for the geometrical shapes of multiple conducting cylinders [17], [18]. The particle swarm optimization (PSO) has been successfully applied in 3-D

Manuscript received September 19, 2019; revised December 7, 2019; accepted December 15, 2019. Date of publication January 17, 2020; date of current version May 5, 2020. This work was supported by the National Key R&D Program of the Ministry of Science and Technology of China under Grant 2018YFF01013300. *(Jiawen Li and Jianliang Zhuo contributed equally to this work.) (Corresponding author: Feng Han.)*

Jiawen Li, Yanjin Chen, and Feng Han are with the Institute of Electromagnetics and Acoustics, Xiamen University, Xiamen 361005, China, and also with the Fujian Provincial Key Laboratory of Electromagnetic Wave Science and Detection Technology, Xiamen University, Xiamen 361005, China (e-mail: feng.han@xmu.edu.cn).

Jianliang Zhuo is with the Postdoctoral Mobile Station of Information and Communication Engineering, Xiamen University, Xiamen 361005, China, and also with the Key Laboratory of Electromagnetic Wave Science and Detection Technology, Xiamen University, Xiamen 361005, China.

Qing Huo Liu is with the Department of Electrical and Computer Engineering, Duke University, Durham, NC 27708 USA (e-mail:qhliu@duke.edu).

Color versions of one or more of the figures in this article are available online at http://ieeexplore.ieee.org.

Digital Object Identifier 10.1109/TMTT.2020.2964772

quantitative MWI [19], [20] and direct retrieval of the locations of 2-D cylindrical scatterers [21]. In addition, the dielectric parameters for a multilayer cylinder were retrieved by the memetic algorithm (MA) [22]. There are also other stochastic methods and their applications for FWI scattering or parameter retrieval are reviewed in [23] and [24] and readers can refer to it. Compared with the deterministic method, the stochastic method can avoid being trapped into local minima of the cost function. However, the dimension of unknown model parameters is severely restricted and thus is especially problematic for the 3-D voxel-based inversion in which the dielectric parameters in all discretized cells are to be reconstructed. This issue has been discussed in [23].

In this article, we use the stochastic method PSO to quantitatively retrieve the composite model parameters of 3-D homogeneous biaxial anisotropic scatterers. Here the "composite" means the model parameters have two kinds. The first one is the dielectric parameter such as relative permittivity, relative permeability, etc. The second one is the angle of the optical axis of a scatterer with respect to the user-defined coordinate. The aim of this article is to provide an alternative way to find all the specific parameters of homogeneous anisotropic objects such as crystals placed in a measurement system with unknown directions of the optical axes through the noncontact detection. Note we assume each unknown object is homogeneous in this article. This is valid in many MWI engineering applications. For example, in the nondestructive testing and evaluation for aging transportation infrastructure, the pavement cracks and black rusts as well as salt rusts are homogeneous [25]. In the MWI measurements for breast cancer, the internal breast structure can be treated as homogeneous due to its high dielectric contrast with respect to the background tissue [26]. When the noninvasive inspection of crystals is implemented in laboratory measurements, the samples are usually assumed homogeneous [27].

Our work is different from [16]–[22] since only the 2-D pixel-based images were reconstructed or multiple model parameters including dielectric constants or geometric parameters were retrieved for isotropic objects although they also used the stochastic method. In the previous work, there was also the reconstruction of anisotropic objects through FWIs [28], [29]. However, the optical axes of the anisotropic objects were assumed to be aligned with the user-defined axes. In [30], although both the dielectric parameters and the angles of the optical axes were simultaneously reconstructed, only the 2-D cases were considered and thus only the value of one angle was retrieved by the deterministic method. In [31], the full symmetrical tensors of 3-D arbitrary anisotropic scatterers were directly reconstructed by the deterministic variational Born iteration method (VBIM) instead of retrieving the diagonal elements of the biaxial tensors and angles of the optical axes. In this article, both the diagonal elements and two optical axis angles of 3-D homogeneous scatterers are simultaneously retrieved by the stochastic method. Therefore, the new contribution of this article is to solve the composite model parameters of homogeneous biaxial objects using the stochastic method. We use the PSO instead of BIM or VBIM to retrieve the composite model parameters due to the complicated nonlinear relationships between the unknown angles of the optical axes and scattered fields measured at the receiver arrays. The nonlinear relationships are mainly manifested by the operations of sinusoidal and cosine functions for the evaluation of the full tensors of the scatterer contrasts with respect to the background medium. When the iterative deterministic method BIM or VBIM is employed, the large discrepancy between the measured scattered field and updated scattered field from the last iteration step leads to extra errors of the solved angles in the current iteration step due to the strong nonlinear relationships between the angles and scattered fields, thus making the whole procedure difficult to converge. The organization of this article is as follows. In Section II, the forward and inversion models and the method adopted to obtain the geometric models of the unknown objects are presented. In Section III, two numerical examples are used to verify the proposed method. In addition, in order to test the adaptability of the algorithm for different angles of the optical axes, we retrieve the model parameters for 60 angle combinations and analyze the errors for different angle values. Finally, in Section IV, conclusions are drawn and discussions are presented.

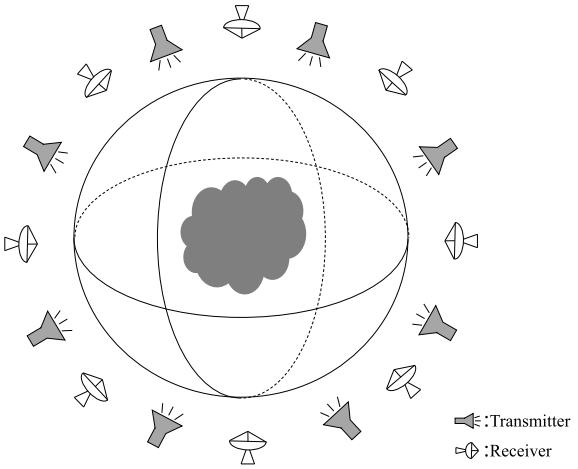

Fig. 1. Illustration of an MWI system.

II. Methods

A typical MWI system is shown in Fig. 1. The transmitters and receivers surrounding the unknown targets are used to emit and receive microwaves. Based on the volume integral equation method, the state equations in the forward model and the data equations in the inversion model are used to retrieve the composite model parameters including angles of the optical axes and the dielectric parameters of the targets. When the geometric models of the targets are unknown, the structural consistency constraint and structural continuity scanning (SCC-SCS) [31] are combined with VBIM to find the spatial geometry shapes of the objects.

A. Angles of the Optical Axes

We assume that the dielectric tensor is diagonalizable and the biaxial objects (scatterers) are placed in air. Their relative

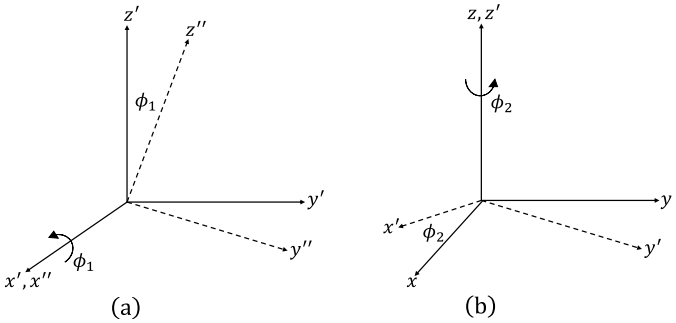

Fig. 2. Two successive rotational transformations to align the principal coordinate $\hat{x}'' - \hat{y}'' - \hat{z}''$ with the user-defined coordinate $\hat{x} - \hat{y} - \hat{z}$.

dielectric parameters are defined as

$$\overline{\overline{\xi}}_s = \begin{bmatrix} \xi_x & 0 & 0 \\ 0 & \xi_y & 0 \\ 0 & 0 & \xi_z \end{bmatrix} = \text{diag}\{\xi_x, \xi_y, \xi_z\} \tag{1}$$

where ξ can be ε, μ, or σ and the subscript s denotes the scatterer. When the optical axis of the object does not coincide with the user-defined coordinate system, we need to make a rotation to align the optical axes with the coordinate axes. However, the dielectric parameters will become a full symmetrical tensor in the user-defined coordinate system. The details of these procedures will be discussed in the following. Fig. 2 shows the rotational transformations. Let $\hat{x}'' - \hat{y}'' - \hat{z}''$ be the principal coordinate system in which the optical axis of the object is aligned with $\hat{z}''$. We then perform two rotational transformations and align $\hat{x}'' - \hat{y}'' - \hat{z}''$ with the user-defined coordinate system $\hat{x} - \hat{y} - \hat{z}$. The dielectric parameter becomes a symmetrical full tensor in $\hat{x} - \hat{y} - \hat{z}$:

$$\overline{\overline{\xi}}'_s = \begin{bmatrix} \xi^s_{11} & \xi^s_{12} & \xi^s_{13} \\ \xi^s_{21} & \xi^s_{22} & \xi^s_{23} \\ \xi^s_{31} & \xi^s_{32} & \xi^s_{33} \end{bmatrix} \tag{2}$$

where $\xi^s_{ij} = \xi^s_{ji}$ with $i, j = 1, 2$ or 3. Its elements are evaluated as [32]:

$$\xi_{11} = \xi_x \cos^2\phi_2 + \xi_y \cos^2\phi_1 \sin^2\phi_2 + \xi_z \sin^2\phi_1 \sin^2\phi_2 \tag{3a}$$

$$\xi_{12} = -\xi_x \sin\phi_2 \cos\phi_2 + \xi_y \cos^2\phi_1 \sin\phi_2 \cos\phi_2 + \xi_z \sin^2\phi_1 \sin\phi_2 \cos\phi_2 \tag{3b}$$

$$\xi_{13} = -\xi_y \sin\phi_1 \cos\phi_1 \sin\phi_2 + \xi_z \sin\phi_1 \cos\phi_1 \sin\phi_2 \tag{3c}$$

$$\xi_{22} = \xi_x \sin^2\phi_2 + \xi_y \cos^2\phi_1 \cos^2\phi_2 + \xi_z \sin^2\phi_1 \cos^2\phi_2 \tag{3d}$$

$$\xi_{23} = -\xi_y \sin\phi_1 \cos\phi_1 \cos\phi_2 + \xi_z \sin\phi_1 \cos\phi_1 \cos\phi_2 \tag{3e}$$

$$\xi_{33} = \xi_y \sin^2\phi_1 + \xi_z \cos^2\phi_1. \tag{3f}$$

In this article, ξ_x, ξ_y, ξ_z in (1) and ϕ_1, ϕ_2 in Fig. 2 are directly retrieved by PSO simultaneously.

B. Forward Model

The forward model is formulated by the state equations which can be expressed as [31]:

$$\begin{aligned} \mathbf{E}_{\text{inc}}(\mathbf{r}) = \mathbf{E}_{\text{tot}}(\mathbf{r}) - \mathbf{E}_{\text{sct}}(\mathbf{r}) = \overline{\overline{\epsilon}}^{-1}(\mathbf{r}) \frac{\mathbf{D}_{\text{tot}}(\mathbf{r})}{\varepsilon_0} \\ - \quad j\omega \int_D \overline{\overline{\mathbf{G}}}_{\mathbf{EJ}}(\mathbf{r}, \mathbf{r}') \cdot \overline{\overline{\chi}}_\epsilon(\mathbf{r}') \mathbf{D}_{\text{tot}}(\mathbf{r}') d\mathbf{r}' \\ - \quad j\omega \int_D \overline{\overline{\mathbf{G}}}_{\mathbf{EM}}(\mathbf{r}, \mathbf{r}') \cdot \overline{\overline{\chi}}_\mu(\mathbf{r}') \mathbf{B}_{\text{tot}}(\mathbf{r}') d\mathbf{r}' \end{aligned} \tag{4a}$$

$$\begin{aligned} \mathbf{H}_{\text{inc}}(\mathbf{r}) = \mathbf{H}_{\text{tot}}(\mathbf{r}) - \mathbf{H}_{\text{sct}}(\mathbf{r}) = \overline{\overline{\mu}}^{-1}(\mathbf{r}) \frac{\mathbf{B}_{\text{tot}}(\mathbf{r})}{\mu_0} \\ - j\omega \int_D \overline{\overline{\mathbf{G}}}_{\mathbf{HJ}}(\mathbf{r}, \mathbf{r}') \cdot \overline{\overline{\chi}}_\epsilon(\mathbf{r}') \mathbf{D}_{\text{tot}}(\mathbf{r}') d\mathbf{r}' \\ - j\omega \int_D \overline{\overline{\mathbf{G}}}_{\mathbf{HM}}(\mathbf{r}, \mathbf{r}') \cdot \overline{\overline{\chi}}_\mu(\mathbf{r}') \mathbf{B}_{tot}(\mathbf{r}') d\mathbf{r}' \end{aligned} \tag{4b}$$

where $\mathbf{E}_{\text{inc}}$ and $\mathbf{H}_{\text{inc}}$ are the incident fields when the scatterers are absent. $\mathbf{D}_{\text{tot}}$ and $\mathbf{B}_{\text{tot}}$ are the total flux densities when the scatterers are present. $\overline{\overline{\mathbf{G}}}_{\mathbf{EJ}}$, $\overline{\overline{\mathbf{G}}}_{\mathbf{EM}}$, $\overline{\overline{\mathbf{G}}}_{\mathbf{HJ}}$, and $\overline{\overline{\mathbf{G}}}_{\mathbf{HM}}$ are the dyadic Green's functions in the homogeneous air. They have analytic expressions [33]. We let (4) be discretized and the total fluxes $\mathbf{D}_{\text{tot}}$ and $\mathbf{B}_{\text{tot}}$ are solved by the stabilized biconjugate-gradient fast Fourier transform (BCGS-FFT) [31], [34], [35]. In the forward computation, the contrasts $\overline{\overline{\chi}}_\varepsilon$ and $\overline{\overline{\chi}}_\mu$ with respect to the background medium parameters ϵ_0 and μ_0 are full tensors which can be derived from (2) and (3) readily.

C. Inversion Model

The inversion model is formulated by the data equations which can be expressed as

$$\begin{aligned} \mathbf{E}_{\text{sct}}(\mathbf{r}) = j\omega \int_D \overline{\overline{\mathbf{G}}}_{\mathbf{EJ}}(\mathbf{r}, \mathbf{r}') \cdot \overline{\overline{\chi}}_\epsilon(\mathbf{r}') \mathbf{D}_{\text{tot}}(\mathbf{r}') d\mathbf{r}' \\ + j\omega \int_D \overline{\overline{\mathbf{G}}}_{\mathbf{EM}}(\mathbf{r}, \mathbf{r}') \cdot \overline{\overline{\chi}}_\mu(\mathbf{r}') \mathbf{B}_{\text{tot}}(\mathbf{r}') d\mathbf{r}' \end{aligned} \tag{5a}$$

$$\begin{aligned} \mathbf{H}_{\text{sct}}(\mathbf{r}) = j\omega \int_D \overline{\overline{\mathbf{G}}}_{\mathbf{HJ}}(\mathbf{r}, \mathbf{r}') \cdot \overline{\overline{\chi}}_\epsilon(\mathbf{r}') \mathbf{D}_{\text{tot}}(\mathbf{r}') d\mathbf{r}' \\ + j\omega \int_D \overline{\overline{\mathbf{G}}}_{\mathbf{HM}}(\mathbf{r}, \mathbf{r}') \cdot \overline{\overline{\chi}}_\mu(\mathbf{r}') \mathbf{B}_{\text{tot}}(\mathbf{r}') d\mathbf{r}' \end{aligned} \tag{5b}$$

where $\mathbf{E}_{\text{sct}}$ and $\mathbf{H}_{\text{sct}}$ are the scattered fields measured at the receiver arrays. In our previous work [31], the full tensors $\overline{\overline{\chi}}_\varepsilon$ and $\overline{\overline{\chi}}_\mu$ are solved from the discretized data equations (5) by VBIM. However, this is feasible only when the off-diagonal elements of the tensor are comparable to the diagonal elements. When the magnitudes of the off-diagonal elements are much smaller than those of the diagonal elements, the off-diagonal elements cannot be reconstructed since their contributions to the scattered fields are negligible compared with those from the diagonal elements. Therefore, in this article, we directly retrieve the model parameters ξ_x, ξ_y as well as ξ_z in (1) and the angles defined in Fig. 2 by the stochastic method PSO. In addition, we assume that each scatterer is homogeneous in the inversion domain and thus has 11 unknowns to be retrieved by the PSO, supposing all ϵ, μ, and σ have the same optical axes. The fitness function

for PSO is the mismatch between the measured and scattered field data and is defined as

$$f = \frac{\|\mathbf{L}' - \mathbf{L}\|}{\|\mathbf{L}'\|} \tag{6}$$

where $\mathbf{L}'$ and $\mathbf{L}$ are column vectors containing the measured scattered field data and the reconstructed scattered field data which are computed from the model parameters for the current particle positions, and $\|\cdot\|$ is the L_2 norm. The column elements of $\mathbf{L}$ and $\mathbf{L}'$ for each frequency are expressed as

$$\mathbf{L}(\omega_i) = \begin{bmatrix} \mathbf{E}_{\text{sct}}(\omega_i) \\ \eta_0 \mathbf{H}_{\text{sct}}(\omega_i) \end{bmatrix} \quad \mathbf{L}'(\omega_i) = \begin{bmatrix} \mathbf{E}'_{\text{sct}}(\omega_i) \\ \eta_0 \mathbf{H}'_{\text{sct}}(\omega_i) \end{bmatrix} \tag{7}$$

where η_0 is the intrinsic impedance of air. The vector $\mathbf{L}'$ is the input of the fitness function (6) which keeps unchanged in the whole process. By contrast, the vector $\mathbf{L}$ is updated in each iteration of BCGS-FFT-PSO. We assume that there are N homogeneous scatterers in the inversion domain, and use M_T transmitters, M_R receivers, and M_F frequencies to perform the retrieval. The dimension of $\mathbf{L}$ or $\mathbf{L}'$ is $6M_TM_RM_F$. By substituting (3) into (5) and dividing the whole inversion domain into $N_x \times N_y \times N_z$ discretized cells, we can obtain the scattered fields

$$\mathbf{E}_{\text{sct}}(\mathbf{r}) = j\omega\Delta V\left(\varepsilon_0 \sum_{\mathbf{i}} \mathbf{A}^{\mathbf{EJ}}\widetilde{\boldsymbol{\epsilon}} + \mu_0 \sum_{\mathbf{i}} \mathbf{A}^{\mathbf{EM}}\boldsymbol{\mu}\right) \tag{8a}$$

$$\mathbf{H}_{\text{sct}}(\mathbf{r}) = j\omega\Delta V\left(\varepsilon_0 \sum_{\mathbf{i}} \mathbf{A}^{\mathbf{HJ}}\widetilde{\boldsymbol{\epsilon}} + \mu_0 \sum_{\mathbf{i}} \mathbf{A}^{\mathbf{HM}}\boldsymbol{\mu}\right) \tag{8b}$$

where $\mathbf{A}$ is a 3×3 matrix. Its elements are functions of Green's functions, the total fields, and ϕ_1 and ϕ_2. The detailed expressions of $\mathbf{A}$ are given in the Appendix. $\mathbf{i} = \{i, j, k\}$ are indexes of the discretized cells in the $\hat{x}$, $\hat{y}$, $\hat{z}$ directions. $\widetilde{\boldsymbol{\epsilon}}$ and $\boldsymbol{\mu}$ are vectors defined as

$$\widetilde{\boldsymbol{\epsilon}} = [\widetilde{\epsilon}_x - \epsilon_b,\ \widetilde{\epsilon}_y - \epsilon_b,\ \widetilde{\epsilon}_z - \epsilon_b]^{\text{T}} \tag{9a}$$

$$\boldsymbol{\mu} = [\mu_x - \mu_b,\ \mu_y - \mu_b,\ \mu_z - \mu_b]^{\text{T}} \tag{9b}$$

where the superscript T denotes matrix transpose, $\widetilde{\boldsymbol{\epsilon}}$ is complex relative permittivity including the conductivity, and ϵ_b and μ_b are equal to 1 in air. $\widetilde{\boldsymbol{\epsilon}}$ and $\boldsymbol{\mu}$ depend on cell index $\mathbf{i}$, i.e., it may change with the spatial position. ΔV is the volume of the discretized cell. Fig. 3 shows the flowchart of BCGS-FFT-PSO. It actually includes two nested loops. The outer loop is the alternate iteration between the forward solver BCGS-FFT and inverse solver PSO. In the forward computation, the model parameters ξ_x, ξ_y, ξ_z, ϕ_1, and ϕ_2 for all the homogeneous scatterers in the inversion domain are known, (3) is used to compute the full tensors of the scatterers, and $\mathbf{D}_{\text{tot}}$ and $\mathbf{B}_{\text{tot}}$ in all the discretized cells are solved from (4) by BCGS-FFT. In the inversion, the PSO is adopted to retrieve the optimal model parameters ξ_x, ξ_y, ξ_z, ϕ_1, and ϕ_2 for all the scatterers by minimizing the fitness function given in (6). This alternate iteration terminates when the mismatch in (6) is smaller than a prescribed threshold or keeps unchanged in several successive iterations. In a certain iteration step of the outer loop BCGS-FFT-PSO, the inner loop of PSO takes 50 iterations to search for the optimum model parameters. Of course we can execute more iterations; however, numerical

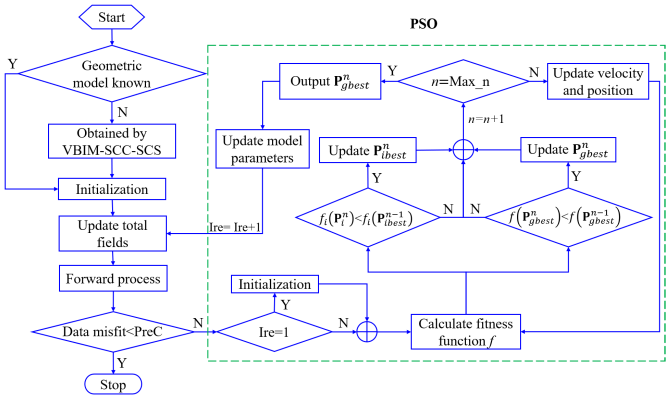

Fig. 3. Flowchart of BCGS-FFT-PSO algorithm. Max_n is the maximum PSO iteration number which is 50 in this article.

examples show that 50 iterations are enough, which will be discussed in Section III. In each iteration of PSO, for the ith single particle, if the value of the fitness function in the nth step is less than the smallest value of that from 1st to $(n-1)$th steps, the optimum position $\mathbf{P}^n_{\text{ibest}}$ for the ith particle is updated by $\mathbf{P}^n_i$. Similarly, the global optimum position $\mathbf{P}^n_{\text{gbest}}$ of the particles can also be updated in the same way. Next, the velocity $\mathbf{V}^{n+1}_i$ and the position $\mathbf{P}^{n+1}_i$ can be updated as follows:

$$W^{n+1}_i = W_{\text{up}} - (n+1)(W_{\text{up}} - W_{\text{down}})/50 \tag{10a}$$

$$\mathbf{V}^{n+1}_i = W^{n+1}_i \mathbf{V}^n_i + C_1 R_1 \left(\mathbf{P}^n_{\text{ibest}} - \mathbf{P}^n_i\right) + C_2 R_2 \left(\mathbf{P}^n_{\text{gbest}} - \mathbf{P}^n_i\right) \tag{10b}$$

$$\mathbf{P}^{n+1}_i = \mathbf{P}^n_i + \mathbf{V}^{n+1}_i \tag{10c}$$

where W^n_i is the weight of the nth step of PSO and is restricted between W_{down} and W_{up}. A larger weight value implies stronger search ability of the particle in the global space, while the smaller weight means the particle has stronger search ability in a local space. The weight is controlled to decrease from W_{up} to W_{down} following (10a) to guarantee the stronger search ability in the global space at the beginning of PSO iterations but stronger search ability in the local space at the end. In this article, W_{up} and W_{down} are empirically chosen as 0.8 and 0.3, respectively. C_1 and C_2 are the learning ratios for an individual particle and the global optimal particle, respectively. They imply how the cognitive and social abilities of a particle take effect in the PSO iterations. If $C_1 = 0$, the particle only has the social ability and thus the PSO only has the global search ability. Its merit is the fast convergence. However, the PSO is easily trapped into a locally optimized solution due to the lack of local search ability. By contrast, when $C_2 = 0$, the particle only has the cognitive ability and the PSO only has the local search ability. Because there is no communication among particles, all the particles search their own optimum solutions independently. As a result, it is very difficult for the PSO to converge to the global minimum. Usually, C_1 and C_2 are set between 0 and 4. In this article, both are chosen as 1.5 empirically. R_1 and R_2 are randomly generated numbers between 0 and 1 which are used to facilitate the random movements of particles.

When the updates in (10) are performed, $\mathbf{V}_i$ is restricted between the range $[\mathbf{V}_{\min}, \mathbf{V}_{\max}]$, and $\mathbf{P}_i$ is restricted between the range $[\mathbf{P}_{\min}, \mathbf{P}_{\max}]$. The $[\mathbf{V}_{\min}, \mathbf{V}_{\max}]$ is also empirically set as $[-0.9, 0.9]$. $[\mathbf{P}_{\min}, \mathbf{P}_{\max}]$ is set as $[0, 6]$ for the relative permittivity and permeability, $[0, 1]$ for the conductivity, and $[0, 360°]$ for the angles ϕ_1 and ϕ_2. We treat the global optimal position as the solutions of the model parameters in the inversion model of (5). Since the PSO algorithm is quite mature, its details will not be discussed any more here. We directly use it to solve an electromagnetic inverse scattering problem in this article. Readers can refer to [36] and [37] for the choice of controlling parameters in PSO.

D. Obtaining the Geometric Model

If the geometric models of the scatterers are unknown, i.e., the spatial locations and shapes are unknown, VBIM-SCC-SCS [31] is used to obtain them before performing the PSO. Although VBIM-SCC-SCS has been directly used to reconstruct all the dielectric parameters of full symmetrical tensors in [31], it is not feasible if the off-diagonal elements are much smaller than the diagonal elements of the full tensor. Such a phenomenon occurs when the rotation angles are not large enough. Numerical computation based on (3) shows that the minimum ratio between the off-diagonal elements and diagonal elements for a certain combination of ϕ_1 and ϕ_2 reaches the maximum value 0.026 when $\phi_1 = \phi_2 = 45°$. For the case $\phi_1 = 5°$ and $\phi_2 = 5°$ which is used in our article, the minimum ratio is around 5×10^{-4}. In this situation, the off-diagonal elements contribute much less to the scattered fields than the diagonal elements contribute. The reconstructed off-diagonal elements from the scattered fields are not reliable, and inferring the rotation angles from the reconstructed off-diagonal elements will cause larger errors. Therefore, VBIM-SCC-SCS is first used to reconstruct all the elements in the full tensor and only the diagonal elements are used to find the geometric models of the objects, and the details are given in [31]. Later, PSO is used to retrieve both the biaxial dielectric parameters and angles. If we have no prior knowledge about the angles or tensor component values, BCGS-FFT-PSO is preferred to VBIM since BCGS-FFT-PSO has a strong adaptability for different rotation angles which will be demonstrated in Section III-B.

III. Numerical Results

In this section, we use two numerical examples to verify the BCGS-FFT-PSO algorithm. In both examples, the background medium is air. The transmitter and receiver arrays are placed on two sides of the unknown objects. In the first example, there is only one biaxial homogeneous scatterer; therefore, there are 11 model parameters to be retrieved. In the second example, there are two biaxial homogeneous scatterers; therefore, there are 22 model parameters to be retrieved. The first example is used to verify the feasibility of the BCGS-FFT-PSO method. The second example is used to test its antinoise ability. The measured scattered field data are synthesized by the forward solver BCGS-FFT. In order to quantitatively evaluate the performance of the proposed method, we define the data misfit and model misfit. The data misfit is the same as the fitness function given in (6). It indicates how well the reconstructed field data match the measured data. The model misfit is defined as

$$\mathrm{Err}_{\mathrm{model}} = \frac{\left|p_i^{\mathrm{ret}} - p_i^{\mathrm{true}}\right|}{p_i^{\mathrm{true}}} \tag{11}$$

where p can be ε, σ, or μ when $i = 1, 2$, and 3 which are corresponding to three components $\hat{x}$, $\hat{y}$, and $\hat{z}$, respectively. p can also be ϕ when $i = 1$ or 2 which is corresponding to the angle ϕ_1 or ϕ_2. The superscript ret stands for the retrieved model parameter; while true means, it is the true parameter. The stop threshold of BCGS-FFT-PSO iteration for the data misfit in (6) is set as 0.1% when the geometric model is known and 1% when the geometric model is unknown. But one should note that BCGS-FFT-PSO will also stop if the data misfit keeps almost unchanged in three successive iterations. All the simulations are run on a workstation with 12-cores Xeon E5-2692 2.2 G CPU, 64 GB RAM.

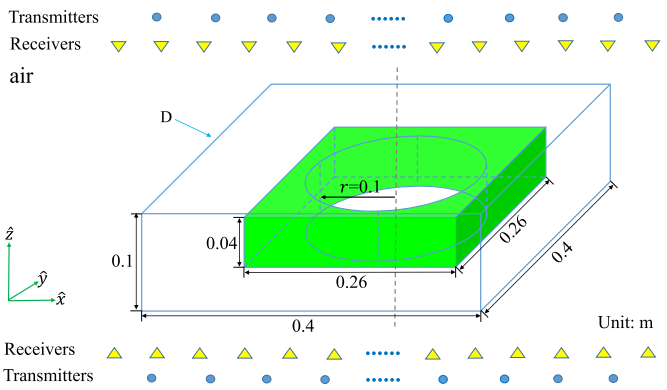

Fig. 4. Configuration of the inversion model with a thin square ring.

TABLE I
True and Retrieved Model Parameters of the Thin Square Ring

Parameter	ε_x	ε_y	ε_z	μ_x	μ_y	μ_z	σ_x	σ_y	σ_z	ϕ_1	ϕ_2
True	1.2	1.5	1.8	1.2	1.3	1.4	5	6	7	30	150
Retrieved-1	1.20	1.50	1.79	1.20	1.30	1.40	5.00	6.00	7.00	29.94	149.98
Retrieved-2	1.19	1.49	1.79	1.19	1.29	1.39	4.98	6.01	7.06	29.69	150.05

Remark: the unit of σ is mS/m; the unit of ϕ is degree; Retrieved-1: geometric model known; Retrieved-2: geometric model unknown.

A. Thin Square Ring

As shown in Fig. 4, a thin square ring is formed by cutting a cylinder with a radius of 0.1 m and height of 0.04 m out of a thin sheet with the dimensions of 0.26 m × 0.26 m × 0.04 m. The model parameters of the biaxial square ring are listed in Table I. The inversion domain D enclosing the object has the dimensions of 0.4 m × 0.4 m × 0.1 m. We divide it into 40 × 40 × 10 cells and the size of each cell is $\Delta x = \Delta y = \Delta z = 0.01$ m. The 72 infinitesimal electric dipole transmitters are uniformly located in two 1.0 m × 1.0 m planes at $z = -0.2$ m and $z = 0.2$ m, respectively. The operating frequency is 800 MHz. The scattered fields are collected by two arrays of 98 receivers uniformly located in two

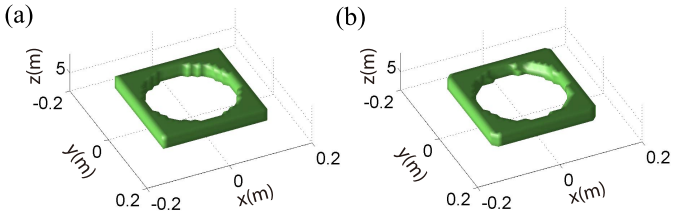

Fig. 5. Iso-surface of the square ring. (a) True geometric model. (b) Geometric model reconstructed by VBIM-SCC-SCS.

1.5 m $\times$ 1.5 m planes at $z = -0.1$ m and $z = 0.1$ m, respectively. The layouts of the transmitter and receiver arrays roughly follow the Nyquist law, i.e., every transmitter or receiver is placed in a half-wavelength space. Fig. 5(a) shows the isosurface of the true geometric model of the thin square ring. When its shape is unknown, VBIM-SCC-SCS is used to obtain the geometric model before performing PSO. The result is shown in Fig. 5(b). Compared with the true model in Fig. 5(a), the edges and corners become smoother. This is caused by the L_2 norm cost function [31]. In addition, numerical simulations show that the reconstructed geometric model of the square ring will become worse if less scattered field data are used in the reconstruction.

Fig. 6 shows the variations in data misfits, model misfits of the dielectric parameters, and the retrieved angles in different iteration steps. We only give the curves for representative components ε_x, μ_y, and σ_z. Other components also have the similar convergence curves and are not displayed here. Several observations are made as follows.

1) The convergence curves show obvious oscillation trends. This is because PSO is a stochastic inversion method. The model parameters updated by the inner loop of PSO are not necessarily the most optimized ones in each BCGS-FFT-PSO iteration. As a result, the data misfit of BCGS-FFT-PSO is not necessarily monotonically descending.
2) The final data misfits and model misfits of the dielectric parameters when the iterations stop are smaller when the geometric model is known compared with those when the geometric model is unknown. However, there is no obvious difference for the retrieved angles. The geometric model acquired by VBIM-SCC-SCS is not exactly the same as the true model, which causes extra errors for the retrieved dielectric parameters by PSO. However, the angles ϕ_1 and ϕ_2 are not sensitive to the small error of the geometric model.
3) When the geometric model is unknown, the final retrieved dielectric parameters do not have the smallest model misfits in the whole iteration processes. Some "background" cells in the geometric model acquired by VBIM-SCC-SCS are actually "scatterer" cells in all the true geometric model. As a result, when the iteration stops, the model misfits are not necessarily the smallest ones in all the iteration steps although the data misfit reaches the minimum.
4) The convergence curves of σ_z shown in Fig. 6(d) are more oscillatory than those shown in Fig. 6(b) and (c) for ε_x and μ_y. This may be due to the fact that the imaginary part of the complex permittivity is much smaller than the real part. The contribution of conductivity to the scattered field is less than those of the permittivity and permeability to the scattered field. Consequently, a small change in the scattered field will lead to more obvious oscillation of the retrieved conductivity during iteration.
5) The retrieved values of ϕ_1 and ϕ_2 are close to the true values several steps before the termination of the iteration. However, the scattered fields are determined by both the dielectric parameters and angles. Only when the data misfits reach the stop criterion can the retrieved ϕ_1 and ϕ_2 come to stable solutions.

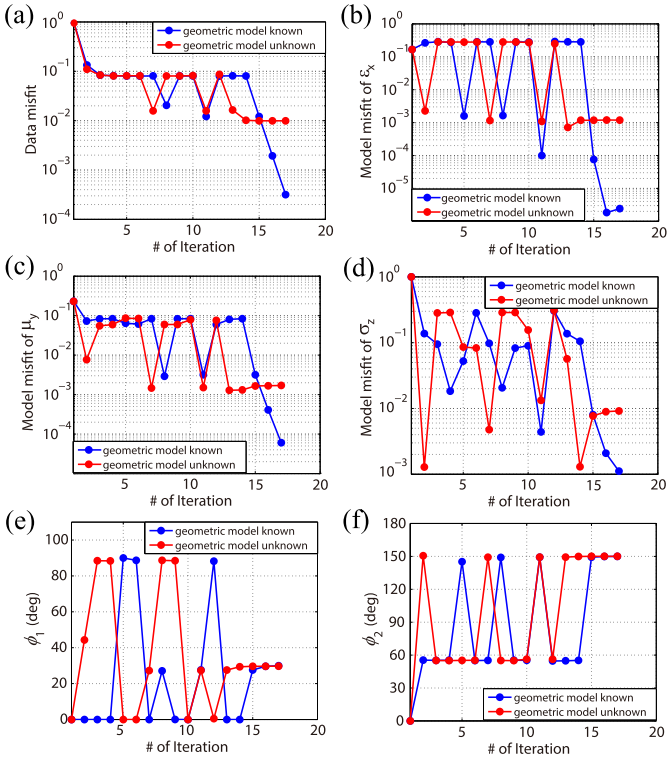

Fig. 6. Convergence curves of BCGS-FFT-PSO. (a) Variations in data misfits in different iteration steps. (b)–(d) Variations in model misfits of dielectric parameters. (e) and (f) Variations in retrieved ϕ_1 and ϕ_2.

The final retrieved model parameters are also listed in Table I. We can see that BCGS-FFT-PSO can retrieve the unknown composite model parameters reliably. Compared with the true parameters, the errors of the retrieval are slightly larger when the geometric model is unknown. The CPU time is 5.5 h for both the known and unknown geometric models.

Fig. 7 shows the contracting processes of different model parameters for the PSO in the last step of the BCGS-FFT-PSO iterations. In the beginning, 500 particles disperse randomly in the whole solution space. As the iteration of PSO proceeds, the particles gradually cluster together and the pattern shrinks to a point. The particle velocity decreases with the iteration. We control this speed reduction in order to make the strong global search ability in the early stage and strong local search ability in the later stage. As shown in Fig. 7(a)–(d), (g)–(j), (m)–(p), and (s)–(v), the particles move fast in first ten

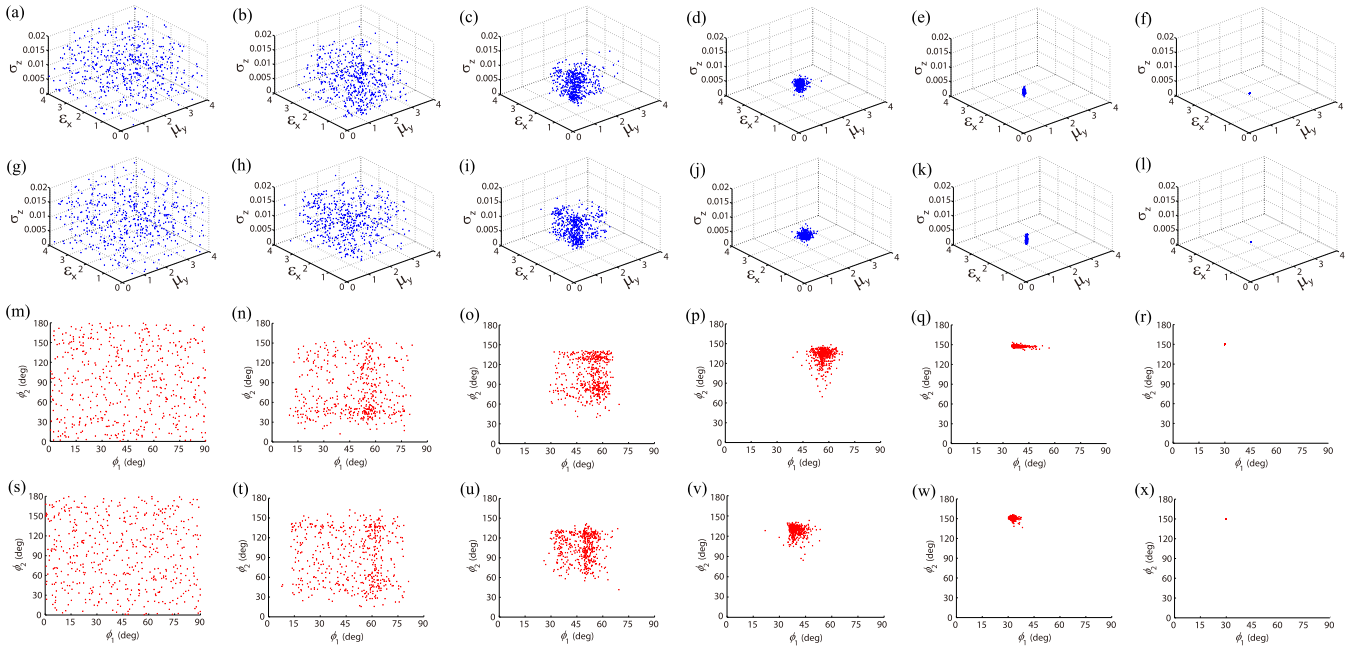

Fig. 7. Spatial positions of particles in different iteration steps of PSO. From left to right, they are 1st, 3rd, 6th, 10th, 20th, and 50th steps. (a)–(f) Dielectric parameters when the geometric model is known. (g)–(l) Dielectric parameters when the geometric model is unknown. (m)–(r) Angles when the geometric model is known. (s)–(x) Angles when the geometric model is unknown. The unit of the conductivity is S/m in (a)–(l).

steps and form the tribes which are shown in Fig. 7(d), (j), (p), and (v). The center of a tribe is near the true position of a dielectric parameter, as shown in Fig. 7(d) and (j). However, the center of the tribe for ϕ_1 or ϕ_2 has some distance from the true value, as shown in Fig. 7(p) and (v). In the following 40 iteration steps, the tribes slowly converge to the true values. These processes are shown in Fig. 7(d)–(f), (j)–(l), (p)–(r), and (v)–(x). Fig. 8 shows the variations in data misfits, model misfits of the dielectric parameters, and retrieved angles in different iteration steps of the PSO. We can see that the data misfits decrease monotonously. This is the merit of PSO. The data misfit of the global optimal solution in the current iteration step is smaller than all the data misfits in all past steps. Meanwhile, due to the inconsistency between the reconstructed geometric model and the true geometric model, the data misfits and model misfits of dielectric parameters are smaller when the geometric model of the scatterer is known compared with those when the geometric model is unknown. In addition, the retrieved model parameters show oscillation trends at the beginning. However, the solutions of both dielectric parameters and angles are stable at the end of the PSO iterations, which are the optimal solutions of the current BCGS-FFT-PSO iteration.

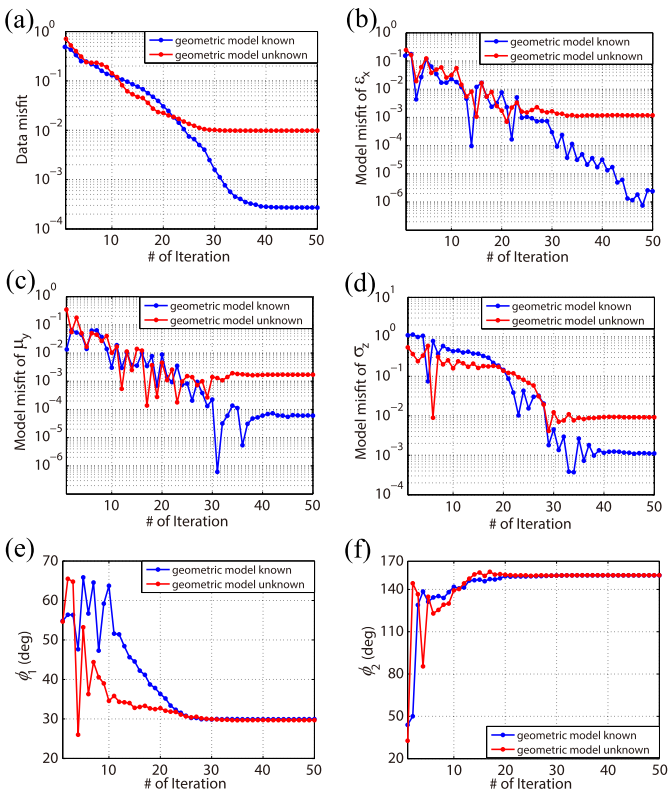

Fig. 8. Convergence curves of PSO iterations. (a) Variations in data misfits in different iteration steps. (b)–(d) Variations in model misfits of dielectric parameters. (e) and (f) Variations in retrieved ϕ_1 and ϕ_2.

B. Validation of Adaptability

In order to test the adaptability of the BCGS-FFT-PSO algorithm for the retrieval of different rotation angles ϕ_1 and ϕ_2, we choose different values of ϕ_1 and ϕ_2 but use the same dielectric parameters as those listed in Table I. Let ϕ_1 take 5°, 10°, 20°, 30°, 45°, 60°, and ϕ_2 take 5°, 10°, 20°, 30°, 45°, 60°, 90°, 120°, 135°, and 150°. Totally, there are 60 combinations. Because the inversion results of these 60 combinations take too much space, we put them in Excel tables in the supplementary material of this article. One should note that $\overline{\overline{\xi}}_s'$ in (2) remains unchanged if we interchange ξ_y and ξ_z

TABLE II
RVR ζ VALUES FOR 60 COMBINATIONS OF ϕ_1 AND ϕ_2

$\zeta(\%)$ ϕ_2 / ϕ_1	5	10	20	30	45	60	90	120	135	150
5	0.191	0.760	2.947	6.297	12.595	18.892	25.190	18.892	12.595	6.297
10	0.503	0.777	3.013	6.438	12.877	19.315	25.754	19.315	12.877	6.438
20	2.170	1.950	3.267	6.981	13.962	20.943	27.924	20.943	13.962	6.981
30	4.810	4.246	4.167	7.813	15.625	23.438	31.250	23.438	15.625	7.813
45	9.772	9.095	8.333	9.375	18.750	28.125	37.500	28.125	18.750	9.375
60	14.734	13.945	12.500	12.500	21.875	32.813	43.750	32.813	21.875	12.500

Remark: the unit of ϕ is degree.

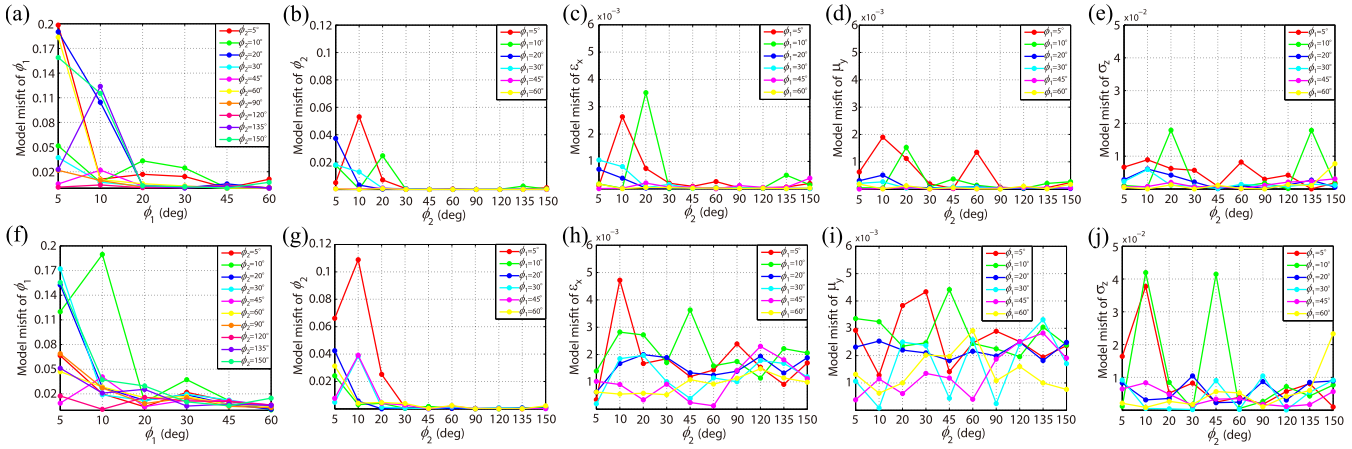

Fig. 9. Final model misfits of the retrieved parameters for 60 different angle combinations when the iterations stop. (a)–(e) Known geometric model. (f)–(j) Unknown geometric model.

and let ϕ_1 increase 90°. Therefore, we restrict the values of ϕ_1 between 0° and 90° to avoid the multiple optimal solutions of PSO. The values of ϕ_2 are restricted between 0° and 180° for the similar reason. In order to facilitate the analysis of the inversion results, we define a new variable, the rotation variation ratio (RVR). It is evaluated by

$$\zeta = \max_{\substack{1 \leqslant i \leqslant 3 \\ p=\varepsilon,\mu,\sigma}} \frac{|p_i' - p_i|}{|\ p_i\ |} \tag{12}$$

where $i = 1, 2$, and 3 are corresponding to $\hat{x}$, $\hat{y}$, and $\hat{z}$ three components, respectively, p represents ε, μ, or σ before the rotation of the optical axis, and p' is the diagonal element after the rotation. The RVR ζ denotes the maximum change in values of diagonal elements after optical axis rotation with respect to those values before the rotation. In the following, we will check how the values of RVR ζ are related to inversion errors of model parameters. The RVR values for different angles of ϕ_1 and ϕ_2 are listed in Table II. We can see that ζ roughly increases with the increment of ϕ_1 or ϕ_2 if their values are less than 90°. When ϕ_2 exceeds 90°, ζ decreases as ϕ_2 increases. This opposite change is caused by the periodicity of sinusoidal and cosine functions of angles. Fig. 9 shows the model misfits of final retrieved parameters for 60 combinations of ϕ_1 and ϕ_2 values. Two observations are made. First, the misfits of model parameters decrease with the increase of ϕ_1 or ϕ_2. When ϕ_1 or ϕ_2 increases, the RVR ζ also increases. It means the rotation of the optical axes influences the scattered fields more obviously. As a result, the model parameters become more sensitive to scattered field variations, and the retrieval errors will decrease. This is clearly shown by comparing Table II and Fig. 9. When $\phi_1 \leqslant 30°$ and $\phi_2 \leqslant 20°$, the RVR ζ is less than 5%. Fig. 9 shows larger model misfits for angles in this range. By contrast, when $\phi_1 > 30°$ or $\phi_2 > 20°$, the model misfits shown in Fig. 9 become smaller. Second, by comparing the curves shown in Fig. 9(a)–(e) with Fig. 9(f)–(j), we can see that the misfits when the geometric model is unknown are obviously larger than those when the geometric model is known. Similar phenomena are also shown in Fig. 6. The inconsistency between the reconstructed geometric model by VBIM-SCC-SCS and the true model causes extra errors for the retrieved model parameters. This is also validated by the final data misfits. As shown in Fig. 10, when the geometric model of the object is unknown, the final data misfits are obviously larger than the misfits when the geometric model is known. The above analysis of the inversion results for the wide ranges of ϕ_1 and ϕ_2 indicates that the proposed BCGS-FFT-PSO has strong adaptability to retrieve the composite model parameters of biaxial objects with different angles of optical axes. We can see that the errors of the retrieved angles are less than 1° and those of retrieved permittivity and permeability values are less than 0.5% for most combinations of ϕ_1 and ϕ_2. The relative errors of retrieved conductivity values are less than 4%. By contrast, VBIM-SCC-SCS proposed in [31] has no such strong adaptability since it cannot reconstruct the

TABLE III
TRUE AND RETRIEVED MODEL PARAMETERS OF THE CUBE AND CUBOID

Values / Parameter / Object		ε_x	ε_y	ε_z	μ_x	μ_y	μ_z	σ_x	σ_y	σ_z	ϕ_1	ϕ_2
cube	True	1.200	1.500	1.800	1.200	1.300	1.400	5.000	6.000	7.000	20.00	45.00
	Noise free	1.202	1.490	1.797	1.203	1.299	1.403	5.163	5.913	6.972	21.23	45.31
	20 dB noise	1.207	1.522	1.833	1.212	1.320	1.420	3.349	6.444	7.412	21.68	45.14
cuboid	True	1.300	1.800	1.400	1.300	1.700	1.200	4.000	7.000	6.000	60.00	130.00
	Noise free	1.295	1.802	1.397	1.299	1.708	1.200	4.140	7.093	6.147	60.48	130.32
	20 dB noise	1.289	1.794	1.385	1.273	1.670	1.188	3.869	7.172	6.440	59.20	128.65

Remark: the unit of σ is mS/m; the unit of ϕ is degree.

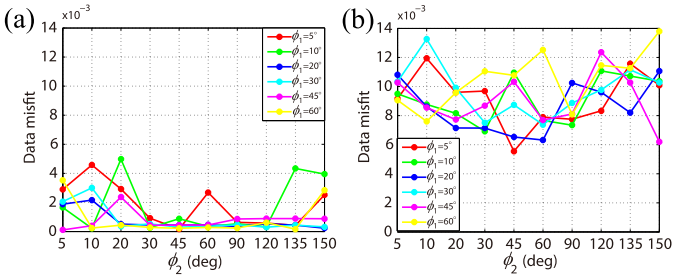

Fig. 10. Final data misfits when the iterations stop for 60 different angle combinations. (a) Geometric model of the object is known. (b) Geometric model of the object is unknown.

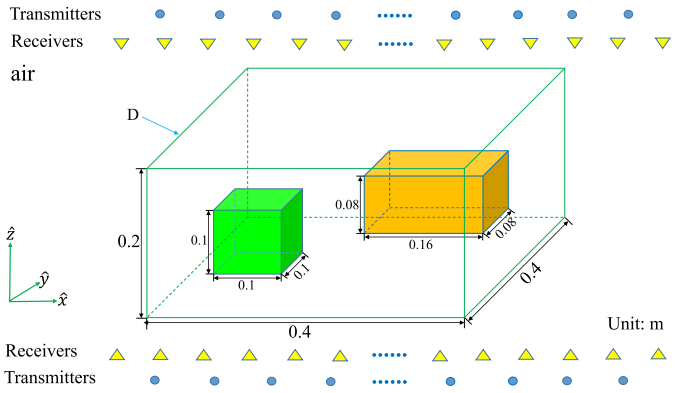

Fig. 11. Configuration of the inversion model with two objects.

small off-diagonal elements of the dielectric tensors when the rotation angles are not large enough.

C. Two Unknown Objects

As shown in Fig. 11, there are two unknown objects in the inversion domain. The cube has the dimensions of 0.1 m × 0.1 m × 0.1 m, and the cuboid has the dimensions of 0.16 m × 0.08 m × 0.08 m. The true model parameters are listed in Table III.

The inversion domain D enclosing the objects has the dimensions of 0.4 m × 0.4 m × 0.2 m and is divided into 40 × 40 × 20 cells. The size of each cell is $\Delta x = \Delta y = \Delta z = 0.01$ m. The 128 transmitters are uniformly located in two 1.4 m × 1.4 m planes at $z = -0.15$ m and $z = 0.15$ m, respectively. The operating frequency is also 800 MHz. The scattered fields are collected by arrays of 128 receivers uniformly located in two 1.5 m × 1.5 m planes at $z = -0.13$ m

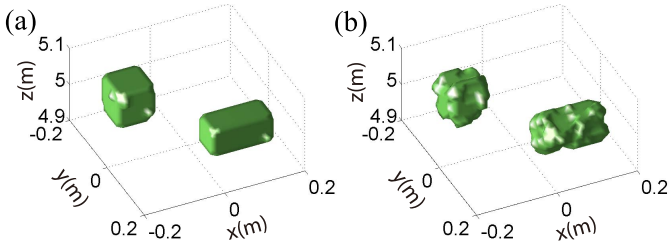

Fig. 12. Geometric models of the cube and cuboid obtained by VBIM-SCC-SCS. (a) Noise free. (b) 20-dB noise added.

and $z = 0.13$ m, respectively. In order to study the antinoise ability of BCGS-FFT-PSO, we retrieve the model parameters of two objects simultaneously. The measured scattered fields are contaminated by 20-dB white Gaussian noise, which leads to approximately 10% errors of the data. Here, the noise level is defined according to the signal-to-noise ratio (SNR) of power. Similar to the last case, we also obtain the geometric models of two objects by VBIM-SCC-SCS before using PSO to solve the model parameters. As shown in Fig. 12, the shapes of the cube and cuboid are distorted when 20-dB noise is added.

Fig. 13 shows the variations in model misfits of the dielectric parameters and retrieved angles in different iteration steps of BCGS-FFT-PSO when noise free and 20-dB noise is added. We can see that the final model misfits of the retrieved dielectric parameters when noise free are obviously smaller. The model misfits of the conductivity are obviously larger than those of permittivity and permeability. Similar phenomenon is also observed in Fig. 6. The retrieved angles ϕ_1 and ϕ_2 are almost not affected by noise. The noise influence is mainly manifested by the dielectric parameters. In addition, we notice that the retrieved model parameters converge faster when noise is added. This is because noise data show randomness. When the data misfit in the iterations reaches the amplitude ratio of noise to signal, it will keep unchanged since it is almost impossible to further adjust the model parameters to match the scattered field data contaminated by random noise. However, the data misfit can keep decreasing to a smaller value when the scattered field data are not affected by noise. This is also obviously illustrated by the variations in data misfits shown in Fig. 14. When 20-dB noise is added, the error of the scattered field is around 10%. When the data misfit approaches 10% in the BCGS-FFT-PSO iteration, it almost remains unchanged and the iteration stops. However, for the

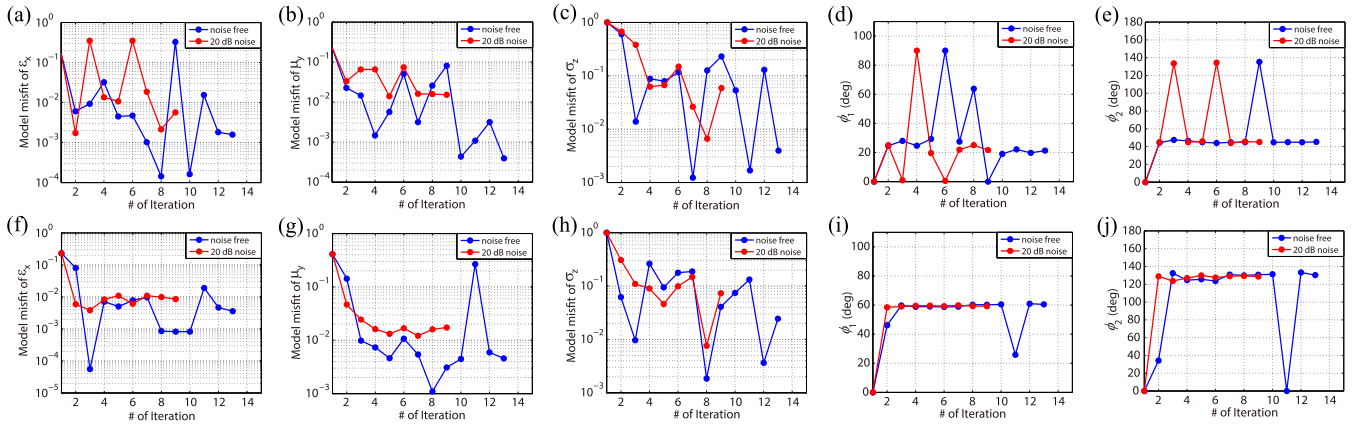

Fig. 13. Comparisons of the variations in model misfits of the dielectric parameters and retrieved angles in different iteration steps of BCGS-FFT-PSO when noise free and 20-dB noise is added. (a)–(e) Cube. (f)–(i) Cuboid.

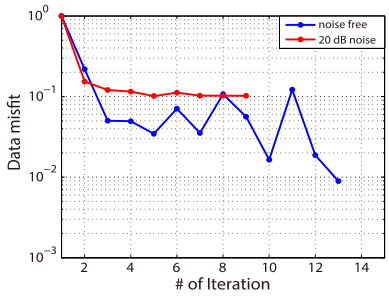

Fig. 14. Comparison of the variations in data misfits in different iteration steps of BCGS-FFT-PSO when noise free and 20-dB noise is added.

noise free data, BCGS-FFT-PSO takes 13 iterations to reduce the data misfit to less than 1%. The final retrieved model parameters are listed in Table III. The CPU time is 17.8 h when noise free but 5.6 h when the 20-dB noise is added. We can see that the retrieved model parameters are close to the true values. Most relative errors are less than 1%. The retrieved angles ϕ_1 and ϕ_2 are very close to the true values. From the above discussions, we conclude that the reconstructed geometric models by VBIM-SCC-SCS are distorted when 20-dB noise is added. However, the retrieved dielectric parameters show errors around 1%. But the noise almost has not effect on the retrieved rotation angles. In addition, numerical simulations show that both the retrieved dielectric parameters and angles have larger errors if we increase the noise level to 10 dB due to the more severely distorted geometric models reconstructed by VBIM-SCC-SCS.

IV. Conclusion

In this article, we present the quantitative MWI of biaxial anisotropic objects placed in the homogeneous air. The optical axes of the objects can be rotated with arbitrary angles. Totally, nine parameters of permittivity, permeability, and conductivity and two arbitrary rotation angles ϕ_1 and ϕ_2 are retrieved. Two sets of model parameters are retrieved simultaneously by the stochastic method PSO. If the geometric models of the objects are unknown, VBIM-SCC-SCS is first employed to obtain them before performing the PSO. Two typical numerical examples are used to verify the performance of the proposed method for MWI of 3-D objects. Both dielectric parameters and rotation angles of optical axes are well retrieved. The proposed method has strong adaptability and is capable of retrieving rotation angles of optical axes in wide ranges with errors less than 1°. The results of the second example show that VBIM-BCGS-PSO has good imaging ability of multiple objects with different dielectric parameters and rotation angles. Meanwhile, its antinoise ability is also confirmed. One may raise the question regarding the practical applications of the proposed algorithm since we assume the multiple unknown objects are homogeneous. As we mentioned in Section II, in many MWI measurements such as nondestructive testing, breast cancer detection, inspection of crystals, etc., the scatterers are sometimes assumed homogeneous. When the scatterers are arbitrarily inhomogeneous, the 3-D voxel-based FWI must be performed to acquire all the model parameters in all the discretized cells. Unfortunately, the stochastic method PSO cannot deal with a huge number of unknown model parameters. On the other hand, the traditional deterministic method such as VBIM supports the high-dimensional vector of the unknowns. However, due to the strong nonlinearity between the measured scattered field data and the angles ϕ_1 and ϕ_2, it is difficult for the VBIM to iteratively find the correct solutions of the angles in all the discretized cells from the measured scattered fields at the receiver arrays.

Appendix

The matrix $\mathbf{A}$ in (8) is expressed as

$$\mathbf{A}^{\mathbf{XY}} = \begin{bmatrix} A_{11}^{\mathrm{XY}} & A_{12}^{\mathrm{XY}} & A_{13}^{\mathrm{XY}} \\ A_{21}^{\mathrm{XY}} & A_{22}^{\mathrm{XY}} & A_{23}^{\mathrm{XY}} \\ A_{31}^{\mathrm{XY}} & A_{32}^{\mathrm{XY}} & A_{33}^{\mathrm{XY}} \end{bmatrix} \tag{13}$$

where **XY** can be **EJ**, **EM**, **HJ**, or **HM**. Each element of $\mathbf{A}^{\mathbf{XY}}$ is computed

$$\begin{aligned} A_{i1}^{\mathrm{XY}} &= g_{i1}^{\mathrm{XY}} F_{\mathrm{tot}}^{x} \cos^2\phi_2 - g_{i2}^{\mathrm{XY}} F_{\mathrm{tot}}^{x} \sin\phi_2 \cos\phi_2 \\ &\quad - g_{i1}^{\mathrm{XY}} F_{\mathrm{tot}}^{y} \sin\phi_2 \cos\phi_2 + g_{i2}^{\mathrm{XY}} F_{\mathrm{tot}}^{x} \sin^2\phi_2 \end{aligned} \tag{14a}$$

$$
\begin{aligned}
&A_{i2}^{\mathrm{XY}} \\
&= g_{i1}^{\mathrm{XY}} F_{\mathrm{tot}}^{x} \cos^2\phi_1 \sin^2\phi_2 + g_{i2}^{\mathrm{XY}} F_{\mathrm{tot}}^{x} \cos^2\phi_1 \sin\phi_2 \cos\phi_2 \\
&\quad - g_{i3}^{\mathrm{XY}} F_{\mathrm{tot}}^{x} \sin\phi_1 \cos\phi_1 \sin\phi_2 + g_{i1}^{\mathrm{XY}} F_{\mathrm{tot}}^{y} \cos^2\phi_1 \sin\phi_2 \cos\phi_2 \\
&\quad + g_{i2}^{\mathrm{XY}} F_{\mathrm{tot}}^{y} \cos^2\phi_1 \cos^2\phi_2 - g_{i3}^{\mathrm{XY}} F_{\mathrm{tot}}^{y} \sin\phi_1 \cos\phi_1 \cos\phi_2 \\
&\quad - g_{i1}^{\mathrm{XY}} F_{\mathrm{tot}}^{z} \sin\phi_1 \cos\phi_1 \sin\phi_2 - g_{i2}^{\mathrm{XY}} F_{\mathrm{tot}}^{z} \sin\phi_1 \cos\phi_1 \cos\phi_2 \\
&\quad + g_{i3}^{\mathrm{XY}} F_{\mathrm{tot}}^{z} \sin^2\phi_1 \qquad (14b)
\end{aligned}
$$

$$
\begin{aligned}
&A_{i3}^{\mathrm{XY}} \\
&= g_{i1}^{\mathrm{XY}} F_{\mathrm{tot}}^{x} \sin^2\phi_1 \sin^2\phi_2 + g_{i2}^{\mathrm{XY}} F_{\mathrm{tot}}^{x} \sin^2\phi_1 \sin\phi_2 \cos\phi_2 \\
&\quad + g_{i3}^{\mathrm{XY}} F_{\mathrm{tot}}^{x} \sin\phi_1 \cos\phi_1 \sin\phi_2 + g_{i1}^{\mathrm{XY}} F_{\mathrm{tot}}^{y} \sin^2\phi_1 \sin\phi_2 \cos\phi_2 \\
&\quad + g_{i2}^{\mathrm{XY}} F_{\mathrm{tot}}^{y} \sin^2\phi_1 \cos^2\phi_2 + g_{i3}^{\mathrm{XY}} F_{\mathrm{tot}}^{y} \sin\phi_1 \cos\phi_1 \cos\phi_2 \\
&\quad + g_{i1}^{\mathrm{XY}} F_{\mathrm{tot}}^{z} \sin\phi_1 \cos\phi_1 \sin\phi_2 + g_{i2}^{\mathrm{XY}} F_{\mathrm{tot}}^{z} \sin\phi_1 \cos\phi_1 \cos\phi_2 \\
&\quad + g_{i3}^{\mathrm{XY}} F_{\mathrm{tot}}^{z} \cos^2\phi_1 \qquad (14c)
\end{aligned}
$$

where $i = 1, 2$, or 3, g_{ij}^{XY} is the element of the 3×3 tensor $\overline{\overline{\mathbf{G}}}_{\mathbf{XY}}$ in (4), and $\mathbf{F}_{\mathrm{tot}}$ is the total field which represents the $\mathbf{E}_{tot}$ or $\mathbf{H}_{\mathrm{tot}}$ when the superscript $\mathbf{Y}$ is $\mathbf{J}$ or $\mathbf{M}$.

REFERENCES

[1] K. Paulsen, S. Poplack, D. Li, M. Fanning, and P. Meaney, "A clinical prototype for active microwave imaging of the breast," *IEEE Trans. Microw. Theory Techn.*, vol. 48, no. 11, pp. 1841–1853, Nov. 2000.

[2] A. Afsari, A. M. Abbosh, and Y. Rahmat-Samii, "A rapid medical microwave tomography based on partial differential equations," *IEEE Trans. Antennas Propag.*, vol. 66, no. 10, pp. 5521–5535, Oct. 2018.

[3] K. Ren, Q. Wang, and R. J. Burkholder, "A fast back-projection approach to diffraction tomography for near-field microwave imaging," *IEEE Antennas Wireless Propag. Lett.*, vol. 18, no. 10, pp. 2170–2174, Oct. 2019.

[4] W. Zhang and A. Hoorfar, "Three-dimensional real-time through-the-wall radar imaging with diffraction tomographic algorithm," *IEEE Trans. Geosci. Remote Sens.*, vol. 51, no. 7, pp. 4155–4163, Jul. 2013.

[5] L. Zhang, H.-L. Li, Z.-J. Qiao, and Z.-W. Xu, "A fast BP algorithm with wavenumber spectrum fusion for high-resolution spotlight SAR imaging," *IEEE Geosci. Remote Sens. Lett.*, vol. 11, no. 9, pp. 1460–1464, Sep. 2014.

[6] G. Jia, M. Buchroithner, W. Chang, and X. Li, "Simplified real-time imaging flow for high-resolution FMCW SAR," *IEEE Geosci. Remote Sens. Lett.*, vol. 12, no. 5, pp. 973–977, May 2015.

[7] D. Henke, E. Mendez Dominguez, D. Small, M. E. Schaepman, and E. Meier, "Moving target tracking in single- and multichannel SAR," *IEEE Trans. Geosci. Remote Sens.*, vol. 53, no. 6, pp. 3146–3159, Jun. 2015.

[8] H. Liu, Z. Long, B. Tian, F. Han, G. Fang, and Q. H. Liu, "Two-dimensional reverse-time migration applied to GPR with a 3-D-to-2-D data conversion," *IEEE J. Sel. Topics Appl. Earth Observ. Remote Sens.*, vol. 10, no. 10, pp. 4313–4320, Oct. 2017.

[9] H. Liu, Z. Long, F. Han, G. Fang, and Q. H. Liu, "Frequency-domain reverse-time migration of ground penetrating radar based on layered medium green's functions," *IEEE J. Sel. Topics Appl. Earth Observ. Remote Sens.*, vol. 11, no. 8, pp. 2957–2965, Aug. 2018.

[10] X. Lu, A. Song, R. Qian, and L. Liu, "Anisotropic reverse-time migration of ground-penetrating radar data collected on the sand dunes in the Badain Jaran desert," *IEEE J. Sel. Topics Appl. Earth Observ. Remote Sens.*, vol. 11, no. 2, pp. 647–654, Feb. 2018.

[11] Q. Huo Liu *et al.*, "Active microwave imaging. I. 2-D forward and inverse scattering methods," *IEEE Trans. Microw. Theory Techn.*, vol. 50, no. 1, pp. 123–133, Jan. 2002.

[12] C. Yu *et al.*, "Active microwave imaging II: 3-D system prototype and image reconstruction from experimental data," *IEEE Trans. Microw. Theory Techn.*, vol. 56, no. 4, pp. 991–1000, Apr. 2008.

[13] M. Ostadrahimi, A. Zakaria, J. Lovetri, and L. Shafai, "A near-field dual polarized (TE–TM) microwave imaging system," *IEEE Trans. Microw. Theory Techn.*, vol. 61, no. 3, pp. 1376–1384, Mar. 2013.

[14] M. Asefi, M. Ostadrahimi, A. Zakaria, and J. Lovetri, "A 3-D dual-polarized near-field microwave imaging system," *IEEE Trans. Microw. Theory Techn.*, vol. 62, no. 8, pp. 1790–1797, Aug. 2014.

[15] M. Azghani, P. Kosmas, and F. Marvasti, "Microwave medical imaging based on sparsity and an iterative method with adaptive thresholding," *IEEE Trans. Med. Imag.*, vol. 34, no. 2, pp. 357–365, Feb. 2015.

[16] M. Pastorino, A. Massa, and S. Caorsi, "A microwave inverse scattering technique for image reconstruction based on a genetic algorithm," *IEEE Trans. Instrum. Meas.*, vol. 49, no. 3, pp. 573–578, Jun. 2000.

[17] A. Qing, C. Kwang Lee, and L. Jen, "Electromagnetic inverse scattering of two-dimensional perfectly conducting objects by real-coded genetic algorithm," *IEEE Trans. Geosci. Remote Sens.*, vol. 39, no. 3, pp. 665–676, Mar. 2001.

[18] R. A. Wildman and D. S. Weile, "Geometry reconstruction of conducting cylinders using genetic programming," *IEEE Trans. Antennas Propag.*, vol. 55, no. 3, pp. 629–636, Mar. 2007.

[19] M. Donelli, D. Franceschini, P. Rocca, and A. Massa, "Three-dimensional microwave imaging problems solved through an efficient multiscaling particle swarm optimization," *IEEE Trans. Geosci. Remote Sens.*, vol. 47, no. 5, pp. 1467–1481, May 2009.

[20] M. Salucci, L. Poli, N. Anselmi, and A. Massa, "Multifrequency particle swarm optimization for enhanced multiresolution GPR microwave imaging," *IEEE Trans. Geosci. Remote Sens.*, vol. 55, no. 3, pp. 1305–1317, Mar. 2017.

[21] S. Caorsi, M. Donelli, A. Lommi, and A. Massa, "Location and imaging of two-dimensional scatterers by using a particle swarm algorithm," *J. Electromagn. Waves Appl.*, vol. 18, no. 4, pp. 481–494, Jan. 2004.

[22] S. Caorsi, A. Massa, M. Pastorino, M. Raffetto, and A. Randazzo, "Detection of buried inhomogeneous elliptic cylinders by a memetic algorithm," *IEEE Trans. Antennas Propag.*, vol. 51, no. 10, pp. 2878–2884, Oct. 2003.

[23] M. Pastorino, "Stochastic optimization methods applied to microwave imaging: A review," *IEEE Trans. Antennas Propag.*, vol. 55, no. 3, pp. 538–548, Mar. 2007.

[24] P. Rocca, M. Benedetti, M. Donelli, D. Franceschini, and A. Massa, "Evolutionary optimization as applied to inverse scattering problems," *Inverse Problems*, vol. 25, no. 12, Dec. 2009, Art. no. 123003.

[25] R. Zoughi, *Microwave Non-Destructive Testing and Evaluation Principles*. Dordrecht, The Netherlands: Kluwer, 2000.

[26] M. Klemm, J. A. Leendertz, D. Gibbins, I. J. Craddock, A. Preece, and R. Benjamin, "Microwave radar-based differential breast cancer imaging: Imaging in homogeneous breast phantoms and low contrast scenarios," *IEEE Trans. Antennas Propag.*, vol. 58, no. 7, pp. 2337–2344, Jul. 2010.

[27] P. P. Natali, L. Montalto, D. Rinaldi, F. Davi, N. Paone, and L. Scalise, "Noninvasive inspection of anisotropic crystals: Innovative photoelasticity-based methods," *IEEE Trans. Nucl. Sci.*, vol. 65, no. 8, pp. 2203–2207, Aug. 2018.

[28] Y. Liu *et al.*, "A frequency-hopping subspace-based optimization method for reconstruction of 2-D large uniaxial anisotropic scatterers with TE illumination," *IEEE Trans. Geosci. Remote Sens.*, vol. 54, no. 10, pp. 6091–6099, Oct. 2016.

[29] J. Zhuo, L. Ye, F. Han, L. Xiong, and Q. H. Liu, "Multiparametric electromagnetic inversion of 3-D biaxial anisotropic objects embedded in layered uniaxial media using VBIM enhanced by structural consistency constraint," *IEEE Trans. Antennas Propag.*, to be published.

[30] K. Agarwal, L. Pan, and X. Chen, "Subspace-based optimization method for reconstruction of 2-D complex anisotropic dielectric objects," *IEEE Trans. Microw. Theory Techn.*, vol. 58, no. 4, pp. 1065–1074, Apr. 2010.

[31] J. Li, J. Zhuo, Z. Guan, F. Han, and Q. H. Liu, "3-D electromagnetic scattering and inverse scattering by magnetodielectric objects with arbitrary anisotropy in layered uniaxial media," *IEEE Trans. Antennas Propag.*, to be published.

[32] S. Mudaliar and J. Lee, "Dyadic Green's functions for a two-layer biaxially anisotropic medium," *J. Electromagn. Waves Appl.*, vol. 10, no. 7, pp. 909–923, Jan. 1996.

[33] W. C. Chew, *Waves and Fields in Inhomogeneous Media*. New York, NY, USA: IEEE, 1995, ch. 7.

[34] F. Han, J. Zhuo, N. Liu, Y. Liu, H. Liu, and Q. H. Liu, "Fast solution of electromagnetic scattering for 3-D inhomogeneous anisotropic objects embedded in layered uniaxial media by the BCGS-FFT method," *IEEE Trans. Antennas Propag.*, vol. 67, no. 3, pp. 1748–1759, Mar. 2019.

[35] Z. Yu, W. Zhang, and Q. H. Liu, "The mixed-order BCGS-FFT method for the scattering of three-dimensional inhomogeneous anisotropic magnetodielectric objects," *IEEE Trans. Antennas Propag.*, vol. 63, no. 12, pp. 5709–5717, Dec. 2015.

[36] J. Kennedy and R. Eberhart, "Particle swarm optimization," in *Proc. IEEE Int. Conf. Neural Netw.*, Piscataway, NJ, USA, 1995, pp. 1942–1948.

[37] F. Marini and B. Walczak, "Particle swarm optimization (PSO). A tutorial," *Chemometrics Intell. Lab. Syst.*, vol. 149, pp. 153–165, Dec. 2015.

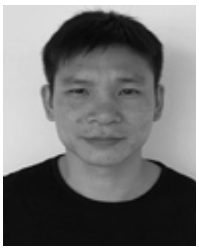

Jiawen Li received the B.S. degree in electronic science and technology from the Wuhan University of Technology of China, Wuhan, China, in 2011. He is currently pursuing the Ph.D. degree with Xiamen University, Xiamen, China.

His research interests include electromagnetic scattering and inverse scattering in complex media and the full-wave inversion of anisotropic targets.

Jianliang Zhuo received the B.S. degree in communication engineering and business administration and the M.S. degree in communication and information system from the University of Electronic Science and Technology of China, Chengdu, China, in 2007 and 2011, respectively, and the Ph.D. degree in physical electronics from Xiamen University, Xiamen, China, in 2018.

Since 2018, he has been a Post-Doctoral Fellow with the Postdoctoral Mobile Station of Information and Communication Engineering, Xiamen University. His research interests include fast forward solvers in electromagnetics and inverse scattering methods for microelectronics and RF systems.

Yanjin Chen received the B.S. degree in mechanical and electronic engineering from the Hainan University of China, Haikou, Hainan, China, in 2017. He is currently pursuing the Ph.D. degree with Xiamen University, Xiamen, China.

His current research interest is applying the machine learning techniques to electromagnetic inverse scattering problems.

Feng Han (Member IEEE) received the B.S. degree in electronic science from Beijing Normal University, Beijing, China, in 2003, the M.S. degree in geophysics from Peking University, Beijing, in 2006, and the Ph.D. degree in electrical engineering from Duke University, Durham, NC, USA, in 2011.

He is currently an Assistant Professor with the Institute of Electromagnetics and Acoustics, Xiamen University, Xiamen, China. His research interests include ionosphere remote sensing by radio atmospherics, electromagnetic full-wave inversion by integral equations, reverse time migration image, and the design of an electromagnetic detection system.

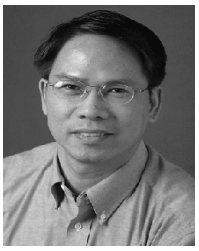

Qing Huo Liu (Fellow IEEE) received the B.S. and M.S. degrees in physics from Xiamen University, Xiamen, China, in 1983 and 1986, respectively, and the Ph.D. degree in electrical engineering from the University of Illinois at Urban–Champaign, Champaign, IL, USA, in 1989.

He was with the Electromagnetics Laboratory, University of Illinois at Urbana–Champaign, as a Research Assistant from September 1986 to December 1988 and as a Post-Doctoral Research Associate from January1989 to February 1990. He was a Research Scientist and the Program Leader with Schlumberger-Doll Research, Ridgefield, CT, USA, from 1990 to 1995. From 1996 to May 1999, he was an Associate Professor with New Mexico State University, Las Cruces, NM, USA. Since June 1999, he has been with Duke University, Durham, NC, USA, where he is currently a Professor of electrical and computer engineering. He has published over 400 articles in refereed journals and 500 articles in conference proceedings. His research interests include computational electromagnetics and acoustics, inverse problems, and their applications in nanophotonics, geophysics, biomedical imaging, and electronic packaging.

Dr. Liu is a Fellow of the Acoustical Society of America, the Electromagnetics Academy, and the Optical Society of America. He also serves as the founding Editor-in-Chief of the new IEEE JOURNAL ON MULTISCALE AND MULTIPHYSICS COMPUTATIONAL TECHNIQUES, the Deputy Editor-in-Chief of *Progress in Electromagnetics Research*, an Associate Editor for the IEEE TRANSACTIONS ON GEOSCIENCE AND REMOTE SENSING, and an Editor for the *Journal of Computational Acoustics*.